RSC Advances

PAPER

View Article Online
View Journal | View Issue

Cite this: *RSC Adv.*, 2025, **15**, 1590

Photocatalytic degradation performance of a chitosan/ZnO–Fe_3O_4 nanocomposite over cationic and anionic dyes under visible-light irradiation

B. M. Quy,[a] N. T. N. Thu,[ab] V. T. Xuan,[a] N. T. H. Hoa,[a] N. T. N. Linh,[a] V. Q. Tung,[a] V. T. T. Le,[c] T. T. Thao,[a] N. T. K. Ngan,[a] P. T. Tho,[de] N. M. Hung[f] and L. T. Ha *[g]

Received 21st November 2024
Accepted 12th January 2025

DOI: 10.1039/d4ra08262a

rsc.li/rsc-advances

The sonochemical synthesis of a chitosan–ZnO/Fe_3O_4 nanocomposite yielded a highly porous structure and large surface area for enhancing the photocatalytic degradation of cationic (rhodamine B, RhB) and anionic (methyl orange, MO) dyes in aqueous solution. Chitosan–ZnO/Fe_3O_4 demonstrated a significant enhancement in photodegradation efficiency 99.49% for MO (C_0 = 5.32 mg L^{-1}, t = 150 min) and 90.73% for RhB (C_0 = 5.03 mg L^{-1}, t = 150 min) under visible light due to its narrow bandgap of 2.84 eV. The photocatalytic performance was investigated by varying the pH, dye concentration, reaction time, and catalyst dose. The photocatalytic reaction obeyed the Langmuir–Hinshelwood kinetic model owing to a high rate constant of 0.031 (min^{-1}) and 0.013 (min^{-1}) for the degradation of MO and RhB, respectively. The photocatalytic activity of the chitosan–ZnO/Fe_3O_4 nanocomposite lost 18.37% (MO degradation) and 11.08% (RhB degradation) of its performance after the first four cycles. The presented results highlight the degradation efficiency of the chitosan–ZnO/Fe_3O_4 nanocomposite under visible light irradiation with reusable and magnetically retrievable abilities.

1. Introduction

Water pollution has emerged as one of the most serious problems with the development of industry, where wastewater contains large amounts of organic dyes, heavy metal ions, and long-chain polymers. When wastewater discharges directly into the environment without adequate treatment, it can lead to a serious threat to the ecosystem and risks to human health *via* the food supply chain.[1–3] Wastewater containing methyl orange or rhodamine B is often found in the textile industry, pharmaceuticals, printing, and other sectors. Excessive exposure to MO can cause skin and eye irritation and lead to bioaccumulation in aquatic organisms.[4] Similarly, RhB is also harmful to human health because of skin irritation, vomiting, and nausea. Long-term exposure to RhB leads to kidney and liver problems. Therefore, it is a mandatory requirement to treat wastewater contaminated by MO and RhB. Methods of wastewater treatment are counting adsorption, photocatalysis, piezocatalysis, electrolysis, biocatalysis, and a combination of them. Photocatalysis is an eco-friendly method because of its ability to decompose harmful dyes into water, carbon dioxide, and nontoxic substances. The degradation of organic dyes under solar light irradiation appears on the surface of the photocatalyst *via* the redox reactions, hence, high efficiency of photocatalysis requests materials with a large surface area, narrow band gap, and low rate of electron–hole recombination.[5] In recent years, ZnO has emerged as a promising semiconductor material for degrading organic dyes in wastewater because of its high degradation efficacy, low cost, and good stability.[6–9] Although the photocatalytic activity of ZnO is good in the UV region, however, it is not good enough in the visible light, which makes it less useful in practice. So, it is needed to extend its performance in the entire solar spectrum by narrowing its band gap energy. Besides, it is also needed to overcome the photo-corrosion and fast recombination of photo-induced charge carriers.[10–13] A hybrid nanostructure of ZnO with other magnetic materials (*e.g.*, Fe_3O_4, $MnFe_2O_4$, MgO, CuO, NiO) provides a versatile method for bandgap engineering, electron–hole pairs separation, and magnetic retrieval.[5,12] For instance, Akshhayya *et al.* reported that the intimate coupling of 3D $MnFe_2O_4$ cubes on 1D ZnO nanorods expanded the absorption region from UV to visible lights; the methylene blue degradation efficiency reached

[a]*Faculty of Chemistry, TNU-University of Sciences, Thai Nguyen 250000, Vietnam*
[b]*Luu Nhan Chu High School, Thai Nguyen 250000, Vietnam*
[c]*Thai Nguyen University of Agriculture and Forestry, Thai Nguyen 250000, Vietnam*
[d]*Laboratory of Magnetism and Magnetic Materials, Science and Technology Advanced Institute, Van Lang University, Ho Chi Minh City, Vietnam*
[e]*Faculty of Applied Technology, School of Technology, Van Lang University, Ho Chi Minh City, Vietnam*
[f]*Department of Chemistry, Faculty of Natural Sciences, Hung Vuong University, Phu Tho 290000, Vietnam*
[g]*Institute of Sciences and Technology, TNU-University of Sciences, Thai Nguyen 250000, Vietnam. E-mail: halt@tnus.edu.vn*

up to 85%, which was higher than that of 63% for pristine ZnO.[14] The combination of ZnO and Fe_3O_4 has received attention in recent years.[12–17] The narrower bandgap of Fe_3O_4 (2.0–2.5 eV) than ZnO (3.37 eV) assures that ZnO/Fe_3O_4 hybrid nanoparticles can be activated in a wider light absorption range, which is beneficial in increasing the number of electron–hole pairs. The research on ZnO/Fe_3O_4 has achieved some prominent results. For example, Huong *et al.* showed that a ZnO/Fe_3O_4 heteronanostructure is efficient for methylene blue degradation of approximately 99.7% under UV light and 79.7% under visible light irradiation.[14] According to Huong *et al.*,[18] the improvement in photocatalytic degradation is due to the increase in the lifetime of electron–hole pairs. Vishwakarma *et al.* synthesized a ZnO/Fe_3O_4 nanocomposite to deal with methyl orange and obtained a degradation efficiency of 84% in 120 minutes under UV light.[15] The above results suggested that ZnO/Fe_3O_4 hybrid structure has the potential to be a good material for the photodegradation of organic dyes. However, both ZnO and Fe_3O_4 still exhibit some drawbacks including photocorrosion,[19,20] particle aggregation, and chemical instability[5,21] that need to be overcome before moving to practical applications.[22,23] In the attempt to avoid oxidation, Fe_3O_4 needs to be shielded from medium; the core/shell structure with Fe_3O_4 as core and ZnO as shell can solve this issue. Unfortunately, the type I core/shell structures of Fe_3O_4/ZnO leads to charge transfer from shell to core.[24] The charge quenching in the Fe_3O_4 core dramatically suppresses the photocatalytic activity of hybrid material.[5] A specific design of nanosheet core/shell heterostructure makes an exception for nonquenching of charge carriers; the defect-induced trapping center at the interface between two materials plays a crucial role for stopping the charge carries flowing into the Fe_3O_4 core.[25] However, controlling the defect chemistry is a big challenge. In general, an extra insulator buffer layer (*e.g.*, SiO_2) is often added between the Fe_3O_4 core and ZnO shell to prevent the charge transfer.[5,21] This kind of structure has low efficiency in the visible light because the Fe_3O_4 core does not join in the photodegradation process.[5] The other promising way is used organic polymer, metal–organic frameworks, or carbon-based materials to capture on ZnO/Fe_3O_4 nanocomposite.[24,25] Nanocomposite of chitosan/ZnO or chitosan/Fe_3O_4 have been widely used in wastewater treatment of various organic dyes.[10,11,26–30] Fe_3O_4/ZnO/chitosan is often synthesized by the coprecipitation method under the influence of ultrasound waves.[31,32] Thanh *et al.* Successfully synthesized Fe_3O_4/ZnO/chitosan, first synthesizing two materials, PEG–Fe_3O_4 and ZnO, separately, then combining these two materials with chitosan solution under the influence of ultrasound.[33] Similarly, Tian *et al.* also proposed a process for synthesizing Fe_3O_4@chitosan@ZnO materials with a core–shell structure under the effect of ultrasound, Fe_3O_4@CS/ZnO by impregnation method.[34] The above synthesis processes are all multi-step, time-consuming synthesis processes. Specifically, it is necessary to synthesize the component materials, such as nano Fe_3O_4 or nano ZnO, separately. The synthesis process takes a lot of time, chemicals, and energy. The composite material in the study allows the Synthesis of CS/ZnO–Fe_3O_4 material in a single reaction vessel, which is simple and saves time, chemicals, and energy. However, the photocatalytic activity of chitosan encapsulated ZnO/Fe_3O_4 is rarely reported. Thus, the current research aims to synthesis chitosan/ZnO/Fe_3O_4 nanocomposite for removal of MO and RhB dyes from aqueous solution under the visible light irradiation. The photodegradation efficiency is about 99.49% for MO and 90.73% for RhB in 150 min. We systematically investigate the photocatalytic performance with varying the pH, dye concentration, reaction time, and catalyst dose. The photocatalytic reaction obeyed the Langmuir–Hinshelwood kinetic model owing to the highly rate constant of 0.031 and 0.013 (min^{-1}) for degradation of MO and RhB, respectively. The photocatalytic activity of chitosan/ZnO–Fe_3O_4 nanocomposite lost 18.37% (MO degradation) and 11.08% (RhB degradation) of its performance after the first four cycles. The presented results highlight the degradation efficiency of chitosan/ZnO–Fe_3O_4 nanocomposite under visible light irradiation with the reusable and magnetically retrievable abilities.

2. Materials and methods

2.1. Materials

The chemicals used in the synthesis of materials include $FeCl_2 \cdot 4H_2O$ (99%), $FeCl_3 \cdot 6H_2O$ (99%), NaOH (99%), CH_3COOH (99%), HCl (37%, $d = 1.19\ g\ mL^{-1}$), $Zn(CH_3COO)_2 \cdot 2H_2O$ (99%), chitosan (DE = 80%), NaCl (99.5%), methyl orange (98.5%), rhodamine B (98.5%). All chemicals utilized in the experiments meet standard requirements for analytical processes. The solutions employed in the study were prepared using double-distilled water.

2.2. Synthesis of materials

The synthesis of composite materials was performed based on the iron synthesis process from Fe_3O_4 oxide. Fe_3O_4 was synthesized using the co-precipitation method with a Fe^{2+}/Fe^{3+} molar ratio of 1 : 2, at pH 13.[35] Initially, 50 mL of Fe^{2+} (0.25 M) and Fe^{3+} (0.50 M) solutions were prepared and dissolved, followed by the gradual addition of a 2 M NaOH solution until the pH reached 13. The synthesis process was conducted in a nitrogen gas environment for 45 minutes at 80 °C. Once the solution turned dark brown and the pH decreased to 7–8, it was transferred to an ultrasonic bath. Next, 20 mL of a 1 M $Zn(CH_3COO)_2$ solution, 10 mL of a 2 M Na_2CO_3 solution, and 25 mL of a chitosan solution (prepared by dissolving 5.46 g of chitosan in 25 mL of 2% acetic acid solution) were slowly added to the reaction mixture. Ultrasonication was performed for 30 minutes at 80 °C. After this, the solution was transferred to a thermostatic water bath and maintained at 100 °C for 60 minutes. The synthesized material was then separated using a magnet and washed 2–3 times with distilled water until the pH reached 7 to eliminate by-products and excess reactants. Finally, the material was dried at 80 °C for 4 hours. The synthesized material is referred to as CS–ZnO/Fe_3O_4.

2.3. Evaluation of material properties

The crystalline structure of the synthesized material was analyzed using X-ray diffraction (XRD) with a D2-Phase instrument (Brucker – Germany). Elemental composition was determined *via* energy-dispersive X-ray spectroscopy (EDS) using a JEOL 5410

instrument (Hitachi – Japan). Morphological characteristics were investigated through scanning electron microscopy (SEM) utilizing a JEOL 1010 instrument (Hitachi – Japan). X-ray photoelectron spectroscopy spectra (XPS, VG Scientific, ESCALAB250). Magnetic properties of materials containing Fe_3O_4 particles were assessed using vibrating sample magnetometry (VSM) on a DMS 880 system (USA). Photoluminescence spectroscopy (PL) was employed to study material lifetime with an FLS 1000 instrument. The bandgap energy was determined using UV-vis diffuse reflectance spectroscopy (UV-vis DRS) with a Shimadzu UV-2600 spectrophotometer.

2.4. The photocatalytic degradation properties of the material

A solution of dye with a volume of 50 mL was introduced into a glass vessel, and the impact of various factors including solution pH (ranging from pH 1 to pH 11), illumination duration (ranging from 5 to 150 minutes), initial dye concentration (ranging from 5 to 40 mg L^{-1}), and mass of the photocatalytic material (ranging from 0.05 to 0.20 grams) on the efficacy of dye treatment was investigated. While examining the influence of individual factors, the remaining variables were held constant. Prior to each photocatalytic degradation experiment, the solution was agitated in darkness for 25 minutes to establish adsorption–desorption equilibrium. Subsequently, the sample was subjected to illumination using a 30 W LED lamp for 150 minutes. At specified intervals of illumination (5, 10, 20, 30, 60, 90, and 150 minutes), 3 mL of the solution was withdrawn, solid residues were eliminated, and the concentration of dye after illumination ($C_{t\text{-ir}}$) was determined using UV-vis spectroscopy. The CS–ZnO/Fe_3O_4 photocatalytic material was isolated using a magnet.

The efficiency of adsorption (RE_{ad}) and photocatalytic degradation (RE) were quantified using the eqn (1) and (2), respectively,

$$RE_{ad} = (C_0 - C_t) \times 100/C_0 \quad (1)$$

$$RE = (C_{0\text{-ir}} - C_{t\text{-ir}}) \times 100/C_{0\text{-ir}} \quad (2)$$

where C_0, C_{ad} (mg L^{-1}) represent the initial and equilibrium concentrations after 25 minutes of adsorption in darkness of the dye solution, RE_{ad} (%) denotes the efficiency of adsorption, and $C_{0\text{-ir}}$, $C_{t\text{-ir}}$ (mg L^{-1}) represent the initial and dye concentration at time t during illumination, and RE (%) signifies the efficiency of photocatalytic degradation.

The concentrations of MO and RhB were determined through UV-vis spectroscopy with wavelengths of maximum absorbance at 663 nm and 554 nm, respectively.

3. Results and discussion

3.1. Material properties

Fig. 1 shows the XRD pattern of CS–ZnO/Fe_3O_4 nanocomposite. The X-ray diffraction (XRD) of nanocomposite material exhibits some distinct diffraction peaks at 2θ angles around 31.68°, 34.37°, 36.08°, 47.46°, 56.55°, 62.76°, 66.28°, 67.87°, and 68.98°. As seen, these peaks are analogous in the peak intensity and peak position of the diffraction profile of the hexagonal wurtzite crystal structure of ZnO. Hence, we identify these peaks to the specific crystal facets: (100), (002), (101), (102), (110), (103), (200), (112), and (201), respectively. Besides the high intense peaks belonging to ZnO, we also observe the subtle peaks at 2θ around 30.32° and 43.21°, which can be assigned to the (220) and (400) reflections of Fe_3O_4.[16,36] The diffraction peak at 2θ = 10.3° signifies the presence of chitosan in the nanocomposite material.[17] The overlap of diffraction peaks at 2θ = 35.6° of Fe_3O_4-(311) with the peak at 36.02° of ZnO-(101) results in the peak broadening for the CS–ZnO/Fe_3O_4 as compared to the pristine ZnO. The XRD analysis confirms the success in the integration of Fe_3O_4, ZnO, and chitosan for forming the composite material CS–ZnO/Fe_3O_4 and underscores the high purity of the synthesized material.

The particle size and surface morphology of CS–ZnO/Fe_3O_4 nanoparticles were observed by SEM images (Fig. 2a) and TEM

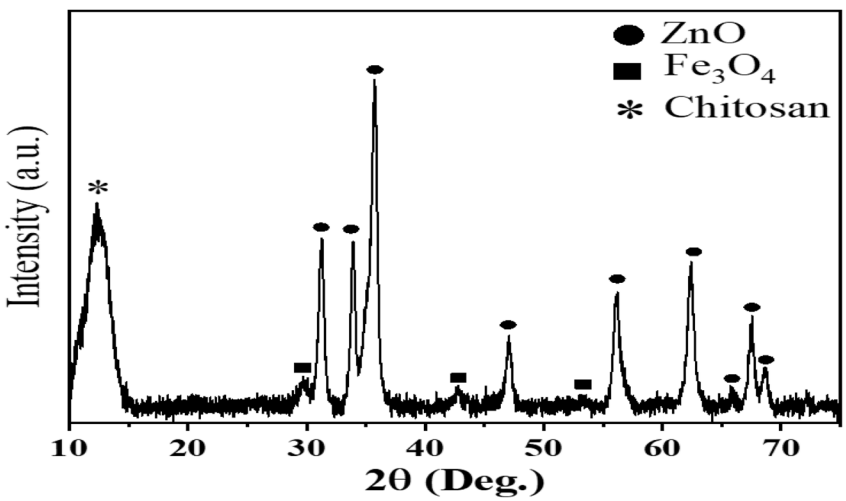

Fig. 1 XRD spectrum of the CS–ZnO/Fe_3O_4 material.

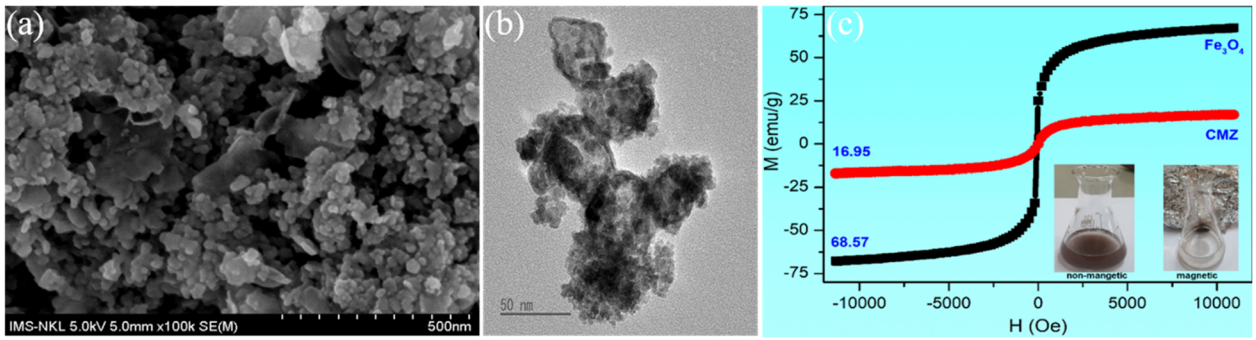

Fig. 2 SEM (a), TEM (b) and VSM (c) images of CS–ZnO/Fe_3O_4.

images (Fig. 2b). The results showed that the average particle size of the material was about 50 nm in diameter. However, the nanoparticles tended to agglomerate into a more extensive cluster due to the magnetic dipole–dipole interaction and/or high reactive surface area that generates van der Waals forces between the nanoparticles. Therefore, the agglomeration of heterogeneous particles creates a porous structure with a larger specific surface area, giving the material a better application adsorption capacity. The magnetic hysteresis loops of both Fe_3O_4 and CS–ZnO/Fe_3O_4 materials indicate the achievement of a saturation magnetization state, as illustrated in Fig. 2c. The magnetic loops have superparamagnetic characteristics with high saturation magnetization and very small coercivity. The saturation magnetization values of Fe_3O_4 and CS–ZnO/Fe_3O_4 are about 68.57 emu g^{-1} and 16.95 emu g^{-1}, respectively. The saturation magnetization of CS–ZnO/Fe_3O_4 was markedly lower than Fe_3O_4 (more than 4 times lower). The magnetic feature of the synthesized materials is desirable for magnetically separable capability.

The EDS analysis in Fig. 3A shows the presence of carbon (C), oxygen (O), iron (Fe), and zinc (Zn) ions as the main elements forming the structure of CS–ZnO/Fe_3O_4. The ratio of the chemical elements determined from the EDX was about 1 : 2 : 4 for C : Fe : Zn. This ratio was very close to the stoichiometric of synthesized material. Furthermore, elemental mapping images of C, O, Fe, and Zn within the specimen exhibited a homogeneous distribution across the entirety of the sample (Fig. 3B).

To elucidate the chemical bonding states within the CS–ZnO/Fe_3O_4 composite, X-ray photoelectron spectroscopy (XPS) was employed. Fig. 4 presents the XPS spectra for CS–ZnO/Fe_3O_4, encompassing a survey scan (a), and specific regions for Fe 2p (b), Zn 2p (c), C 1s (d), N 1s (e), and O 1s (f). The broad survey in Fig. 4a (0–1300 eV) reveals distinct peaks for Zn, Fe, C, N, and O, each in their respective ionic forms. Detailed analysis in Fig. 4b of the Fe 2p region indicates three prominent peaks at 710.55, 723.72, and 740.71 eV, attributed to Fe $2p_{3/2}$, Fe $2p_{1/2}$, and the Fe satellite band.[37,38] Deconvolution of Fe 2p yields six peaks at 708.76, 713.01, 719.52, 724.01, 728.00, and 740.62 eV, where

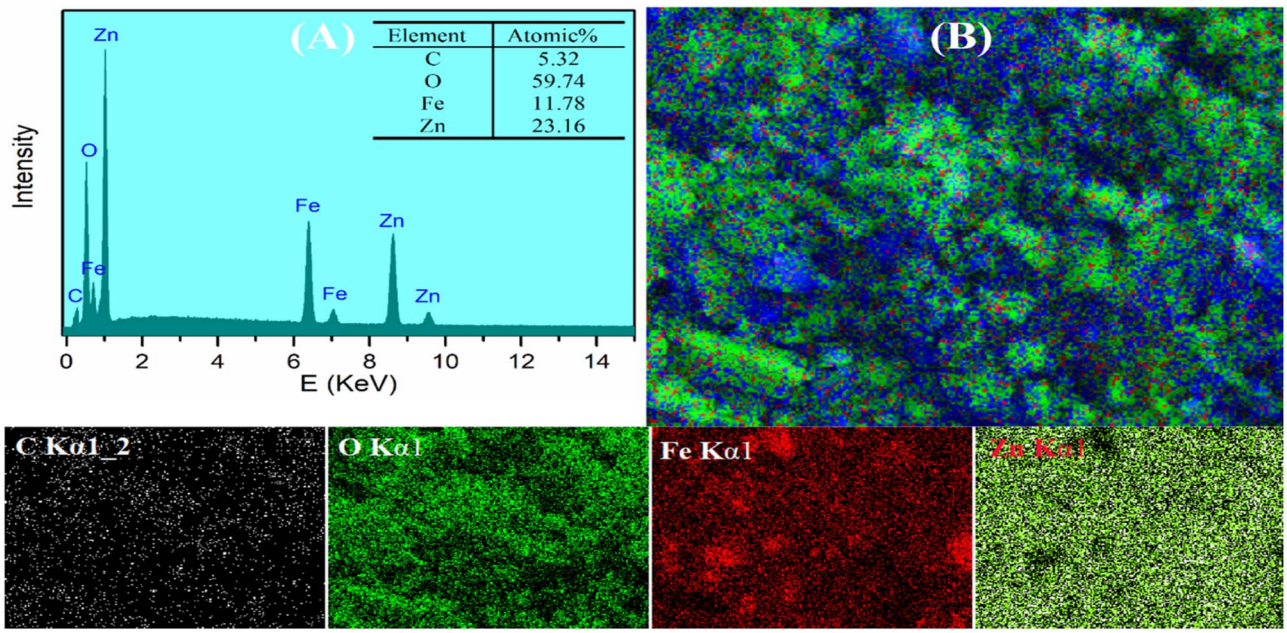

Fig. 3 EDS analysis (A) and elemental mapping analysis of CS/ZnO–Fe_3O_4 (B).

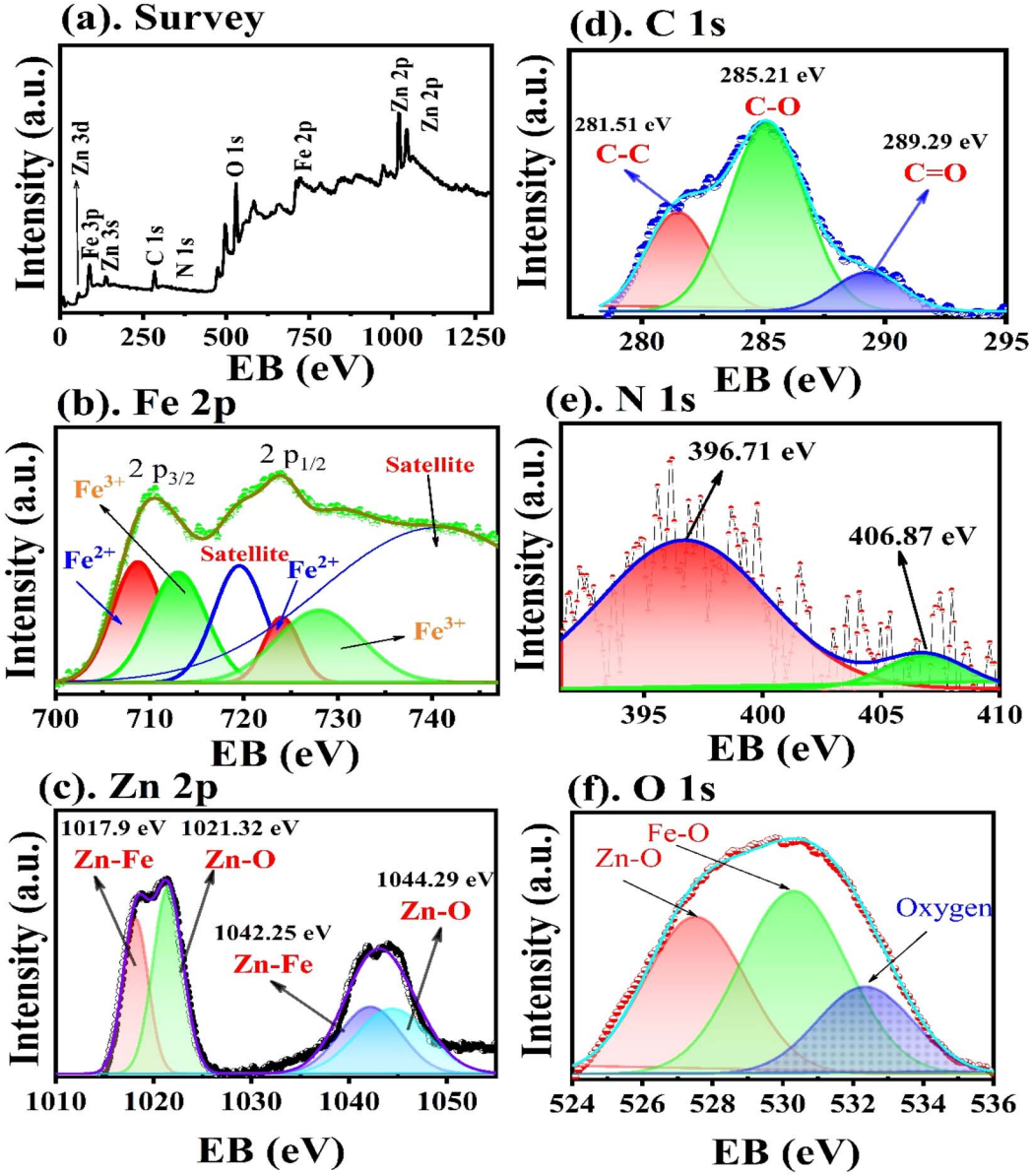

Fig. 4 XPS spectra of CS–ZnO/Fe_3O_4 samples: (a) survey spectrum, (b) Fe 2p, (c) Zn 2p, (d) C 1s, (e) N 1s, (f) O 1s levels.

peaks at 708.76 and 724.01 eV correspond to Fe^{2+} $2p_{3/2}$ and $2p_{1/2}$ states, and 713.01 and 728.00 eV correspond to Fe^{3+} ions. Satellite peaks at 719.52 and 740.62 eV confirm Fe_3O_4 formation and purity, with higher intensity attributed to ZnO–Fe_3O_4 interface defects.

The formation of Fe^{2+} and Fe^{3+} defects within the ZnO matrix likely enhances visible-light absorption by reducing the band gap and improving photocatalytic performance and stability. This is consistent with UV-vis and lifetime analyses (Fig. 5 and 15).

In Fig. 4c, the Zn 2p spectrum exhibits two prominent peaks representing Zn $2p_{3/2}$ and Zn $2p_{1/2}$, with clear separation into four peaks at 1017.90, 1021.32, 1042.25, and 1044.29 eV. Peaks at 1021.32 and 1044.29 eV align with Zn–O bonding, while 1017.90 and 1042.25 eV signify ZnO–Fe_3O_4 hybridization, indicative of successful composite formation. Fig. 4d shows the C 1s spectrum with a main peak at 285.21 eV and shoulders at 281.51 and 289.29 eV, attributed to C–O, C–C, and C=O bonding from chitosan. Fig. 4e further confirms chitosan's incorporation *via* the N 1s state. Fig. 4f presents the O 1s spectrum, featuring peaks at 527.61, 530.27, and 532.41 eV, linked to Zn–O, Fe–O bonds, oxygen defects, and surface-adsorbed oxygen (OH– and carbonate groups from chitosan). Peaks at 527.61 and 532.41 eV correspond to Zn–O bonding and defect states, with the 530.27 eV peak related to Fe–O bonding. In sum, the XPS results confirm the successful synthesis of the CS–ZnO/Fe_3O_4 composite, evidenced by C 1s and N 1s peaks from chitosan and Fe^{2+}/Fe^{3+} defect states within ZnO. These interactions and electron transfer processes between ZnO and

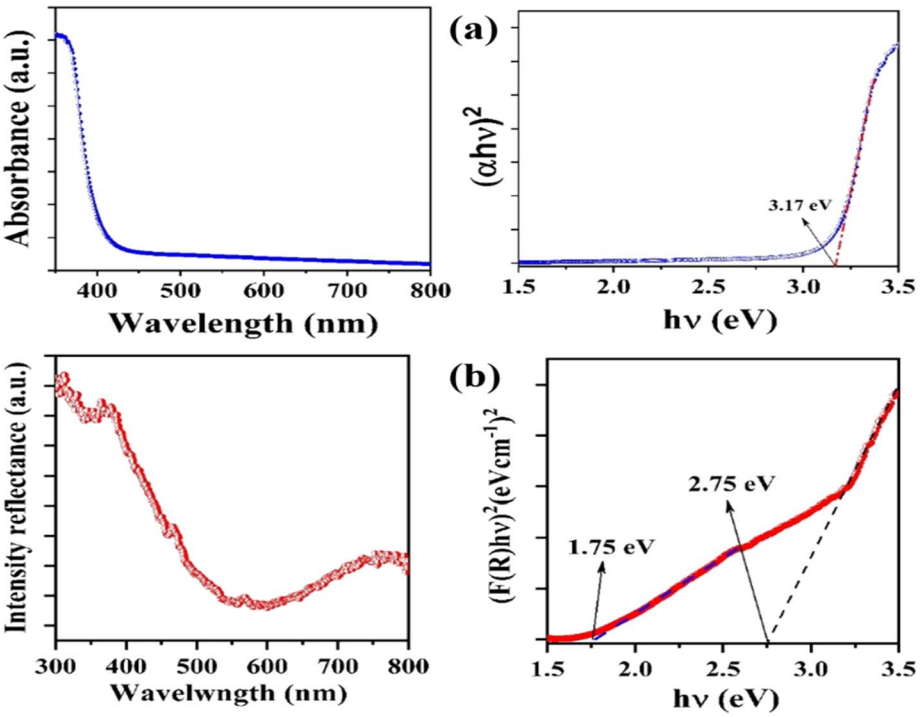

Fig. 5 Relationship between $h\nu$ and $(\alpha h\nu)^2$ of ZnO, $h\nu$ (a), and $(F(R_\infty)h\nu)^2$ of ZnO/Fe_3O_4/chitosan (b).

Fe_3O_4 enhance both absorption and photocatalytic capabilities relative to ZnO alone.

The band gap of ZnO and CS–ZnO/Fe_3O_4 materials was deduced from the UV-vis spectrum according to the Tauc equation and Kubelka–Munk:[39]

$$(\alpha h\nu)^\gamma = A(h\nu - E_g) \quad (3)$$

$$(F(R_\infty)h\nu)^\gamma = A(h\nu - E_g) \quad (4)$$

where α and $h\nu$ are the absorption coefficient and photon energy, and $F(R)$ is the Kubelka–Munk function, respectively, in the % reflectance obtained. A is a characteristic constant of the specific material, respectively. The value of n is dependent on the origin of transition in a semiconductor ($\gamma = 1/2$ and 2 for indirect transition, respectively and allowed direct transition). In our case, $\gamma = 2$ because ZnO and Fe_3O_4 are direct semiconductors. Hence, E_g value of all samples could be calculated by plotting $(\alpha h\nu)^2$ *versus* $h\nu$, as illustrated in Fig. 5. The calculated bandgap energy of ZnO and CS–ZnO/Fe_3O_4 in Fig. 5 are about 3.17 and 2.75 eV, respectively, which are relatively close to reported values. There are two different absorption bands in CS–ZnO/Fe_3O_4, corresponding to the band gap of ZnO and Fe_3O_4, as shown in Fig. 5b. Compared with pure ZnO NPs, the bandgap energy of CS–ZnO/Fe_3O_4 presents a redshift.

3.2. Examining the photocatalytic degradation of MO and RhB by CS–ZnO/Fe_3O_4

3.2.1. Influence of pH. The influence of the pH of the aqueous solution on the degradation performance of CS–ZnO/Fe_3O_4 is shown in Fig. 6. In the process of MO treatment, the adsorption efficiency in the dark condition for 25 minutes is slightly varied in the acidic media (pH = 1–6), ranging from 69.25 to 74.70%. While subsequent exposure under the light results in a notable change in the efficiency; the photocatalytic efficiency is about 18.77% at pH = 6 and then continuously increases to a maximum value of 89.61% at pH = 3 and then decreases down to 38.09 at pH = 1. As seen, the total efficiency of both the adsorption and photocatalysis varied in the range of 78.735% to 97.37%. On the contrary, the adsorption and photocatalytic efficiencies are very low in the neutral and alkaline environments (pH = 7, 8, 9). Interestingly, the efficiency in removing RhB from aqueous solution is in reverse order as compared to removing MO. The overall removal efficiency at the neutral and alkaline pH values (pH = 7, 8, 9) is exceeded over the acidic pH values (pH = 1–6). In acidic conditions, the highest RhB adsorption efficiency was observed at 17.23% (pH = 5), whereas in basic conditions, it peaked at 24.15% (pH = 8). The highest RhB photocatalytic treatment efficiency is at 36.18% under acidic conditions (pH = 6) and 48.59% under basic conditions (pH = 8). The contrary in the removal efficiency of CS–ZnO/Fe_3O_4 against MO and RhB in acidic and neutral/alkaline media can be elucidated by considering the electrostatic interaction between dye molecules in the solution and the surface of the photocatalytic material.

The point of zero charge (pHpzc) of the CS–ZnO/Fe_3O_4 material is around 6.49, as seen in Fig. 7. MO and RhB are known as two typical anionic and cationic dyes, respectively. When the pH of the aqueous solution is smaller than 6.49, the positive charge on the surface of CS–ZnO/Fe_3O_4 readily attracts the MO^- molecules and repels the RhB^+ molecules, thereby

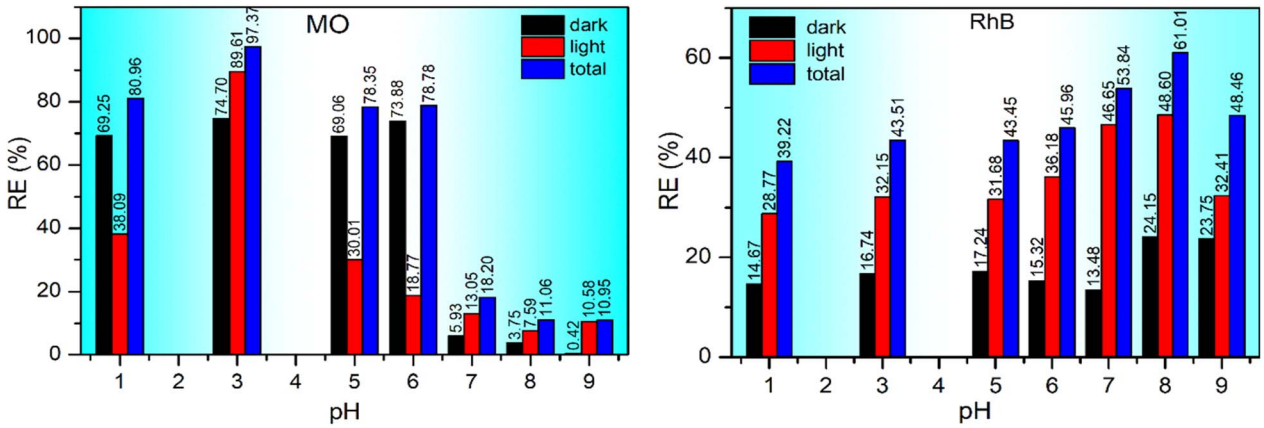

Fig. 6 Influence of pH on the treatment efficiency of MO and RhB by CS/ZnO–Fe_3O_4.

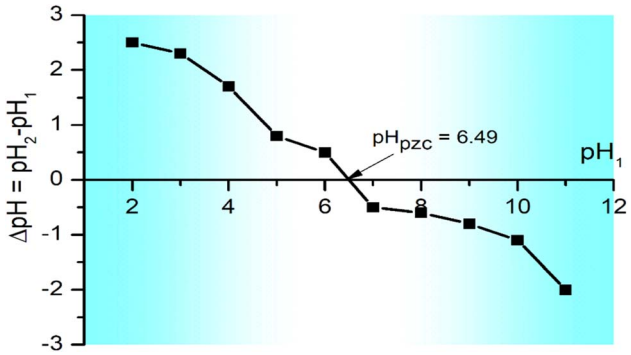

Fig. 7 Point of zero charge of CS–ZnO/Fe_3O_4.

enhancing the adsorption of MO molecules in acidic environments. Conversely, if the pH is greater than 6.49, the negatively charged surface of CS–ZnO/Fe_3O_4 attracts the RhB^+ molecules and repels the MO^- molecules, thus promoting the adsorption of RhB molecules in basic environments. This facilitates the degradation of these substances through photocatalysis on CS–ZnO/Fe_3O_4 under light exposure. In both procedures, the efficacy of dye treatment *via* dark adsorption markedly influenced the overall treatment efficiency of the entire process, underscoring the dual role of the CS–ZnO/Fe_3O_4 material as both an adsorbent and a photocatalyst for degrading cationic (RhB^+) and anionic (MO^-) pollutants. The optimum condition to obtain a maximum removal efficiency is at pH = 3 for MO and pH = 8 for RhB. Accordingly, these pH levels were selected as the experimental conditions for exploring the factors affecting the degradation process in subsequent studies.

3.2.2. Influence of initial dye concentration and illumination duration. The degradation kinetics of MO and RhB were investigated over a time ranging from 0 to 150 minutes. The initial concentration of MO varied between 5.32 and 39.57 mg L^{-1}, while the initial concentration of RhB was in the range of 5.03 to 42.43 mg L^{-1}. Results are shown in Fig. 8. As seen, the degradation efficiency of MO and RhB depends on the initial dye concentration and the duration of illumination. The degradation rates of MO and RhB were increased with prolonged light exposure. Conversely, the escalated initial dye concentration reduces the degradation rate. Specifically, the degradation efficiencies of MO under 150 minutes of visible light illumination were decreased from 99.49% to 78.42% as the initial concentration varied from 5.32 to 39.57 mg L^{-1}.

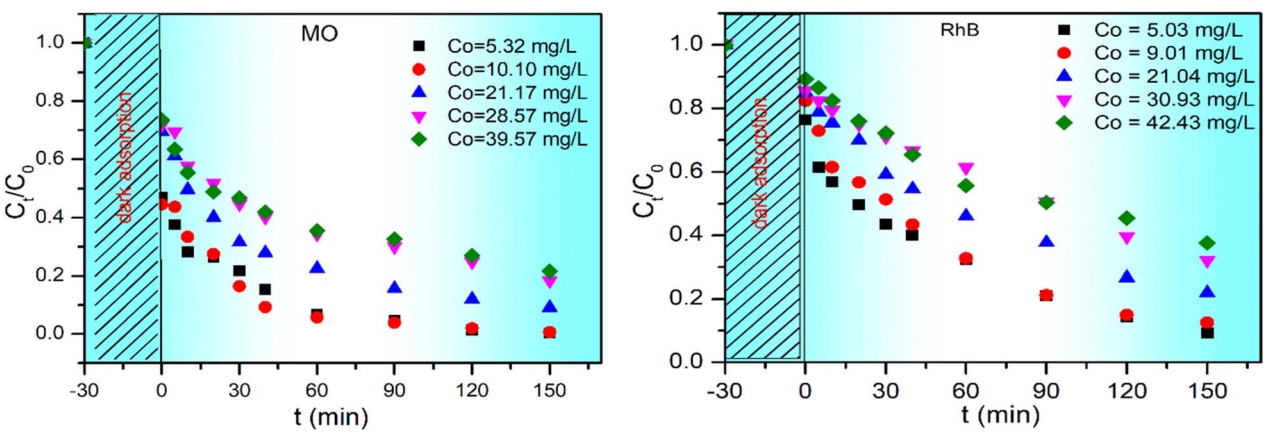

Fig. 8 Temporal degradation profiles of MO and RhB by CS–ZnO/Fe_3O_4 composite material at varied initial concentrations.

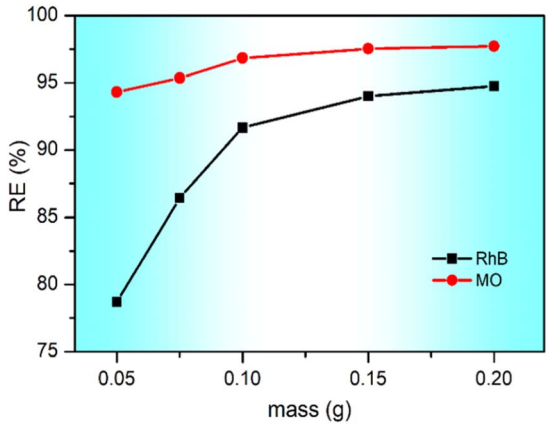

Fig. 9 Degradation efficiency of MO and RhB by CS–ZnO/Fe_3O_4.

Similarly, the degradation efficiencies of RhB under 150 minutes of visible light illumination reduced from 90.73% to 62.39% as the initial concentrations changed from 5.03 to 42.43 mg L^{-1}. After 60 minutes for MO and 90 minutes for RhB, a slight decrease in the degradation rate is observed. This phenomenon was ascribed to the rise in adsorbed compounds on the CS–ZnO/Fe_3O_4 photocatalyst's surface, resulting in reduced degradation.

Moreover, the escalated concentrations of MO and RhB led to an increase in the adsorption of various intermediates on the CS–ZnO/Fe_3O_4 photocatalyst's surface. Consequently, these intermediates compete with MO and RhB for surface adsorption sites on CS–ZnO/Fe_3O_4, retarding the degradation of both substances. Similar findings are reported in the influence of time and pollutant concentration on the photocatalytic efficacy of diverse photocatalytic materials, including phenol and benzoic acid degradation on ZnO,[40] RhB degradation on activated carbon composite materials derived from banana peels and g-C_3N_4,[41] and sulfamethazine degradation by TiO_2.[42] Fig. 8 illustrates that the concentration of both MO and RhB was diminished within 30 minutes of adsorption in darkness. Thus, besides the photocatalytic ability, CS–ZnO/Fe_3O_4 exhibits dye adsorption capabilities on its surface. This adsorptive property of the material further enhances the photocatalytic efficiency of dye degradation in water.

3.2.3. The influence of material mass. To prevent the excess use of catalyst, it is imperative to ascertain the ideal mass of the CS–ZnO/Fe_3O_4 photocatalytic material. The removal efficiency was investigated by varying the mass of CS–ZnO/Fe_3O_4 in the range of 0.05 to 0.20 g. Meanwhile, the dye concentration was kept constant. The influence of CS–ZnO/Fe_3O_4 mass on the photocatalytic degradation performance is shown in Fig. 9 for both MO and RhB. As seen, the degradation of RhB increased quickly with increasing the mass of CS–ZnO/Fe_3O_4, while the mass of CS–ZnO/Fe_3O_4 had less influence on the degradation efficiency of MO. The improvement in efficacy is due to the proliferation of active sites on the CS–ZnO/Fe_3O_4 surface, especially in the range of 0.05 to 0.10 g. When the mass of CS–ZnO/Fe_3O_4 continuously increases from 0.10 to 0.20 g, the degradation efficiency still increases albeit at a very low rate. This phenomenon may stem from the limitation of the light penetration into the solution. The dark brown coloration of CS–ZnO/Fe_3O_4 was also affected by light penetration. The optimized mass for better degradation performance must be chosen between 0.1 and 0.15 g. Accordingly, 0.15 g of CS–ZnO/Fe_3O_4 was utilized for subsequent investigations.

3.3. The kinetics of the photocatalytic degradation process

Utilizing the experimental outcomes from the photocatalytic degradation of MO and RhB on the CS–ZnO/Fe_3O_4 substrate, the degradation kinetics were assessed employing the Langmuir–Hinshelwood pseudo-first-order kinetic model.[7] The findings are exhibited in Fig. 10 and Table 1 and calculated as eqn (5):

$$\ln\frac{C_0}{C_t} = k_{ap}t \tag{5}$$

where: C_0, C_t (mg L^{-1}) are the initial concentration and concentration at time t of the dye solution, and k_{ap} is the reaction rate constant (min^{-1}).

The findings indicate that, within the examined concentration range, the Langmuir–Hinshelwood kinetic model provided a robust description of the experimental data, exhibiting high

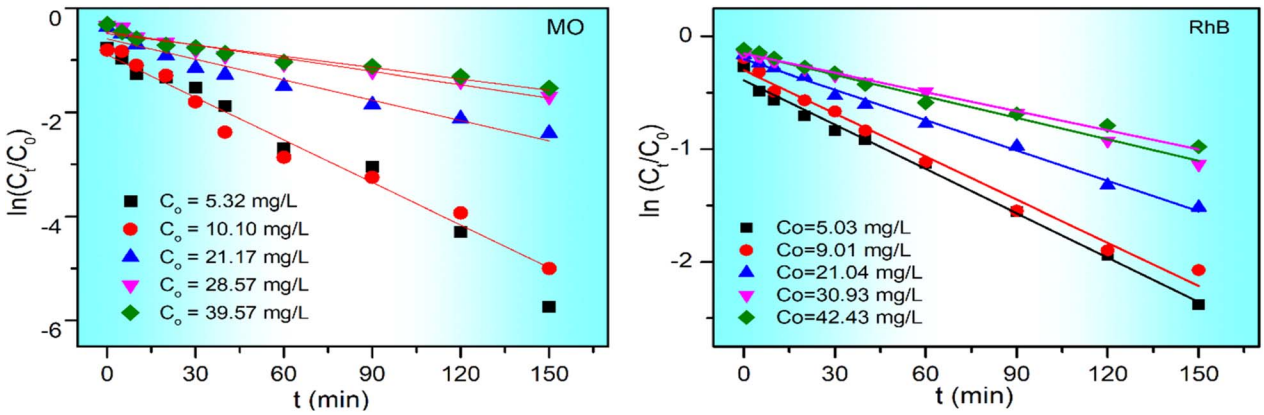

Fig. 10 Langmuir–Hinshelwood kinetic model for MO and RhB treatment using CS–ZnO/Fe_3O_4.

Table 1 Experimental Langmuir–Hinshelwood kinetic equations and parameters in the model

Initial concentration, C_0 (mg L^{-1})	Kinetic equation	k_{ap} (min^{-1})	R^2
MO			
5.32	$\ln(C_t/C_0) = -0.031t - 0.729$	0.031	0.98
10.10	$\ln(C_t/C_0) = -0.027t - 0.729$	0.027	0.97
21.17	$\ln(C_t/C_0) = -0.013t - 0.591$	0.013	0.95
28.57	$\ln(C_t/C_0) = -0.008t - 0.453$	0.008	0.95
39.57	$\ln(C_t/C_0) = -0.007t - 0.490$	0.007	0.95
RhB			
5.03	$\ln(C_t/C_0) = -0.013t - 0.389$	0.013	0.99
9.01	$\ln(C_t/C_0) = -0.012t - 0.299$	0.012	0.99
21.04	$\ln(C_t/C_0) = -0.009t - 0.203$	0.009	0.99
30.93	$\ln(C_t/C_0) = -0.006t - 0.150$	0.006	0.99
42.43	$\ln(C_t/C_0) = -0.005t - 0.154$	0.005	0.98

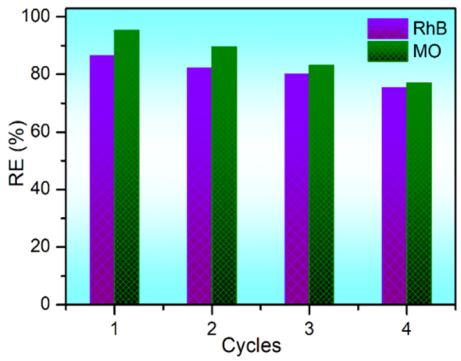

Fig. 11 Efficiency of MO and RhB treatment after re-used cycles.

correlation coefficients ($R^2 = 0.95$–0.99). With increasing initial dye concentrations, the reaction rate constants declined. Specifically, for C_0, MO = 5.31–39.57 mg L^{-1}, the MO degradation rate constant diminishes from 0.031–0.007 min^{-1}; for C_0, RhB = 5.03–42.43 mg L^{-1}, k_{ap}, RhB = 0.013–0.005 min^{-1}. The higher degradation rate constant of MO on CS–ZnO/Fe_3O_4 compared to RhB may be ascribed to MO's lower molecular weight, enhancing its permeation into CS–ZnO/Fe_3O_4 pores and surface adsorption, thereby facilitating a more efficient photocatalytic degradation process than RhB.

The degradation rate constant values for MO in this investigation exceed those reported for MO degradation *via* photocatalysis on Fe_3O_4/ZnO materials synthesized by Joun Xia *et al.* ($k_{ap} = 0.002$ min^{-1})[43] and O. Dlugosz *et al.* ($k_{ap} = 0.001$ min^{-1}).[44] Additionally, the reaction rate constant for RhB degradation by MoS_2 nanosheets synthesized by Liu *et al.* ($k_{ap} = 0.002$ min^{-1})[45] was inferior to the value obtained in this study.

Preliminary findings from the investigation into the photocatalytic degradation of MO and RhB using CS–ZnO/Fe_3O_4 suggest the potential applicability of CS–ZnO/Fe_3O_4 material in the treatment of dye pollutants employing photocatalytic techniques (Fig. 11).

3.4. Assessment of CS–ZnO/Fe_3O_4 material's reusability

The evaluation of CS–ZnO/Fe_3O_4 capacity for repeated use is pivotal in gauging its practical utility. This feature was explored through experimental iterations involving the reapplication of the catalyst material. CS–ZnO/Fe_3O_4 was recurrently employed in batch experiments aimed at eliminating dye contaminants. After each experiment, CS–ZnO/Fe_3O_4 was retrieved from the reaction mixture using a magnet, subjected to triple washing with hot water, and subsequently dried at 60 °C for 8 hours. Photocatalytic degradation trials were carried out under optimized conditions for MO and RhB treatments. Fig. 12 delineates the reutilization potential of CS–ZnO/Fe_3O_4 across four cycles, depicting dye degradation efficiencies of 95.35%, 89.54%, 83.12%, and 76.98% (for MO), and 86.43%, 82.24%, 79.98%, and 75.35% (for RhB), respectively. Notably, CS–ZnO/Fe_3O_4 maintained its photocatalytic degradation prowess post-reuse, albeit exhibiting a marginal decline in efficacy following four cycles. This decrement was ascribed to factors such as the depletion of catalytic particles during retrieval and drying processes, along with the occlusion of active sites owing to CS–ZnO/Fe_3O_4's interaction with the dye molecules.[46–48] In essence, these findings underscore the resilience and reusability of CS–ZnO/Fe_3O_4 in the photocatalytic abatement of dye pollutants.

After each cycle, the CS–ZnO/Fe_3O_4 composite material (CZF) was recovered, and the structural changes of the material were examined by X-ray diffraction. The results of this change in Fig. 12 showed no significant change in the CS–ZnO/Fe_3O_4 composite material structure. The photo dissolution phenomenon with ZnO in this three-component composite material can be explained that in the multi-component structure of ZnO with chitosan and Fe_3O_4 when photoexcited, the electrons in the conduction band of ZnO are transferred to the conduction band of Fe_3O_4 with the redox couple Fe^{3+} and Fe^{2+}. This process increases the electron–hole pair's lifetime, increasing the material's photocatalytic ability. In addition, the presence of chitosan-coated on the surface of ZnO/Fe_3O_4 nanoparticles can transfer photoexcited electrons from the conduction band of ZnO to the conduction band of Fe_3O_4, which improves the conversion rate of Fe^{3+} ions to Fe^{2+} ions in Fe_3O_4. At the same time, combining ZnO with chitosan ZnO with Fe_3O_4 also reduces the band gap of ZnO material, giving the material a more substantial absorption capacity in the visible region. In contrast, the non-radiative recombination process of electrons

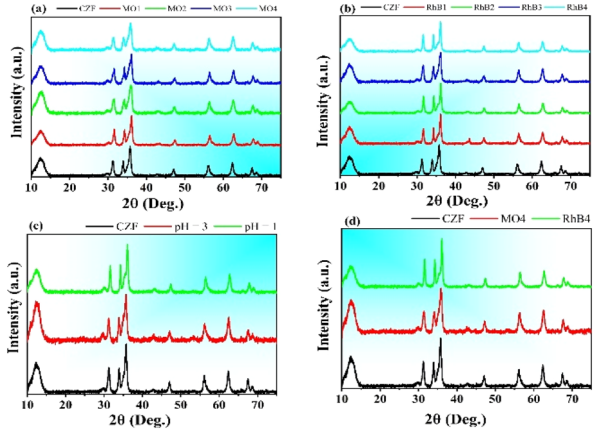

Fig. 12 X-ray diffraction patterns of CS–ZnO/Fe_3O_4 composite materials after each photocatalytic cycle, (a) with MO dye, (b) with RhB dye, (c) effect of pH on the structure after photocatalysis, (c) structure of the material at the 4th cycle with MO and RhB.

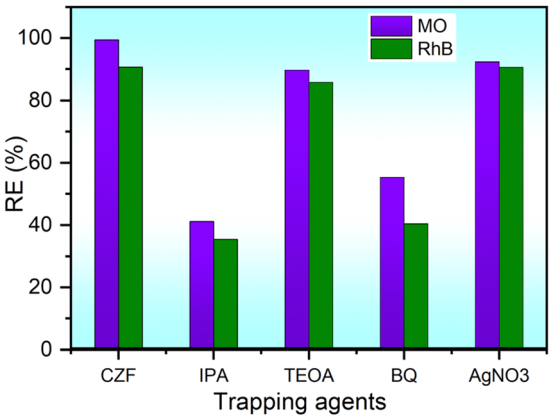

Fig. 13 The degradation efficiency of MO and RhB with trapping agents.

in the conduction band of ZnO material to these doped centers significantly reduces the photo corrosion of ZnO material when excited.

The results affirm that the CS–ZnO/Fe_3O_4 composite material has very high stability and that almost no photocatalytic dissolution phenomenon occurs during the photocatalytic process under optimal conditions.

3.5. The mechanism of photocatalytic degradation

Experiments with radical trapping agents were performed to determine the role of active substances in dye degradation. Isopropyl alcohol (IPA), triethanolamine (TEOA), *p*-benzoquinone (BQ), and $AgNO_3$ were used as trapping agents for hydroxyl radicals (·OH), holes (h^+), superoxide ($*O_2^-$) and electrons,[45,49] respectively. The results are shown in Fig. 13. After introducing radical trapping agents into the photocatalytic reaction, the degradation efficiency decreased, specifically the observed efficiencies were 99.49, 41.25, 89.74, 55.36 and 92.41% (with MO), 90.73, 35.47, 85.93, 40.52 and 90.67% (with RhB) for the reaction without trapping agents, IPA, TEOA, BQ and $AgNO_3$. This study confirmed that hydroxyl radicals (·OH) and superoxide ($*O_2^-$) played a significant role in the degradation of the dyes.

The photocatalytic activity of the CS–ZnO/Fe_3O_4 composite is initiated upon the absorption of electromagnetic radiation, which induces the generation of electron–hole pairs, with electrons transitioning to the conduction band and holes remaining in the valence band. The mechanism underlying this electron–hole pair formation is detailed in eqn (6). Excited electrons in the conduction band subsequently interact with surface oxygen atoms of the CS–ZnO/Fe_3O_4, resulting in the formation of amino radicals incorporating oxygen atoms in an excited state. Concurrently, the valence band holes react with hydroxyl groups, leading to the production of numerous excited-state hydroxyl groups. The processes responsible for the generation of these excited-state oxygen and hydroxyl species are elucidated in eqn (7) and (8).

$$\text{CS/ZnO–Fe}_3\text{O}_4 + h\nu \rightarrow e^-(\text{CB}) + h^+(\text{VB}) \quad (6)$$

$$e^- + O_2 \rightarrow *O_2^- \quad (7)$$

$$h^+ + OH^- \rightarrow *OH \quad (8)$$

Furthermore, valence band holes may react with water molecules, producing excited-state hydroxyl groups, as detailed in eqn (7).

$$h^+ + H_2O \rightarrow *OH + H^+ \quad (9)$$

The degradation of organic dyes is heavily influenced by the interaction of these excited-state oxygen and hydroxyl species with the dye molecules. The degradation mechanism is illustrated through the following equations:

$$*OH + \text{MO} \rightarrow CO_2 + H_2O + \text{degradation products} \quad (10)$$

$$*O_2^- + \text{MO} \rightarrow CO_2 + H_2O + \text{degradation products} \quad (11)$$

$$*OH + \text{RhB} \rightarrow CO_2 + H_2O + \text{degradation products} \quad (12)$$

$$*O_2^- + \text{RhB} \rightarrow CO_2 + H_2O + \text{degradation products} \quad (13)$$

The degradation rate of organic dyes such as MO and RhB was largely influenced by the electron density in the conduction band and the presence of holes in the valence band. Thus, to optimize the photocatalytic degradation of these dyes, it is crucial to preserve the excited state of the electron–hole pairs or ensure the stability of their recombination state.

To further elucidate the optical properties of the CS–ZnO/Fe_3O_4 composite, the band gap energy (E_g) of both ZnO and CS–ZnO/Fe_3O_4 was assessed through the application of the Kubelka–Munk equation. The results presented in Fig. 5 illustrate the relationship between $(\alpha h\nu)^2$ and $(h\nu)$ for the ZnO and CS–ZnO/Fe_3O_4 samples, yielding band gap values of 3.17 eV and 2.75 eV, respectively. This finding indicated a reduction in the band gap of the CS/ZnO–Fe_3O_4 composite compared to the initial ZnO material, thereby enhancing its absorption capability within the visible spectrum. Additionally, the potential

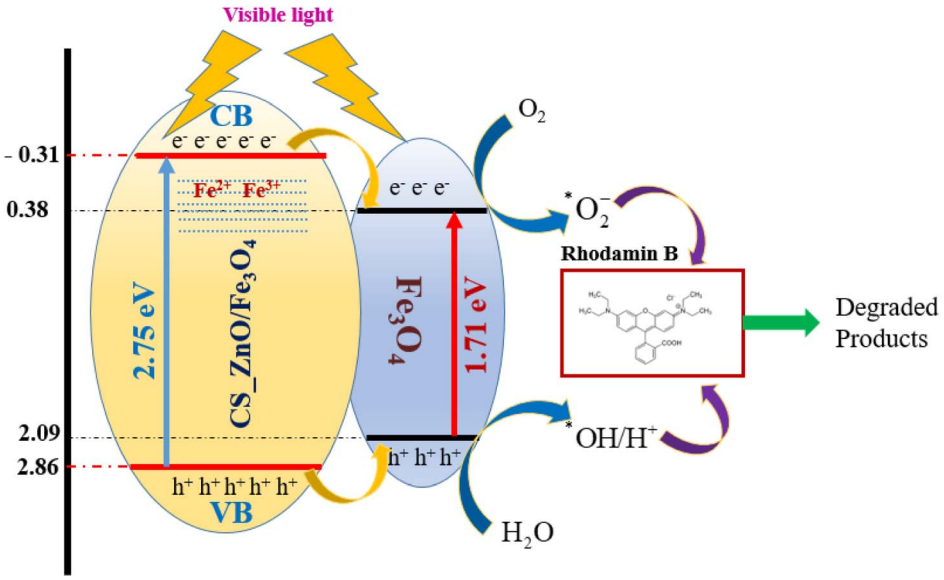

Fig. 14 RhB degradation mechanism of CS–ZnO/Fe_3O_4 when excited by visible light.

energy levels of the valence band (E_{VB}) and conduction band (E_{CB}) for ZnO and CS–ZnO/Fe_3O_4 were calculated using eqn (14) and (15), as employed by Hoai Linh Pham *et al.*[50]

$$E_{CB} = X - E^e - \frac{1}{2}E_g \quad (14)$$

$$E_{VB} = E_g + E_{CB} \quad (15)$$

where, X represents Mulliken's absolute electronegativity, while E_g denotes the band gap energy of the materials. E^e refers to the energy of free electrons on the hydrogen scale, which is 4.5 eV. For ZnO and CS–ZnO/Fe_3O_4, the electronegativity values are 5.78 eV and 5.73 eV, respectively.[25] The calculated conduction band (E_{CB}) and valence band (E_{VB}) values are approximately −0.31 eV and 2.86 eV for ZnO, and 0.375 eV and 2.085 eV for Fe_3O_4, respectively. This information provides insights into the potential charge transfer mechanisms in CS/ZnO–Fe_3O_4.

The mechanism of charge transfer within the material upon excitation, as well as the associated photocatalytic process, is depicted in Fig. 14. Upon exposure to ultraviolet radiation, electrons migrate from the valence band maximum of ZnO to the conduction band minimum, resulting in the generation of electron–hole pairs.

The mechanism of charge transfer within the CS–ZnO/Fe_3O_4 composite material upon excitation and the related photocatalytic process is illustrated in Fig. 14. Upon absorption of visible light, electrons move from the top of the valence band of the CS–ZnO/Fe_3O_4 material to the bottom of the conduction band, resulting in the formation of electron–hole pairs. In ZnO, the recombination of these electron–hole pairs is rapid and characterized by a short lifetime, which contributes to the reduction of its photocatalytic performance, and the material is susceptible to photo corrosion. In contrast, the CS–ZnO/Fe_3O_4 composite material exhibits good radiation absorption in both the ultraviolet and visible regions. Electrons can absorb energy to move to the conduction bands of ZnO and Fe_3O_4 and then relax to energy levels associated with defects in the ZnO lattice or trap levels caused by interface interactions between ZnO and Fe_3O_4 as well as by the doping of Fe ions in the ZnO structure. This non-radiative recombination process significantly reduces the recombination of electrons and holes, thereby prolonging the lifetime of excited-state charge carriers and enhancing the efficiency of the photocatalytic process.

To further confirm this, we measured the lifetime of the ZnO and CS–ZnO/Fe_3O_4 nanoparticles mentioned above. The results showed that the electron lifetime in ZnO was approximately 0.69 ns, while in the CS–ZnO/Fe_3O_4 composite material, this lifetime reached 884.44 μs (Fig. 15). The increase in the lifetime of these excited charge carriers increases the interaction time of electrons with oxygen radicals and holes with hydroxyl groups, leading to the generation of more superoxide and hydroxyl anions, thereby improving the photocatalytic performance of the material. In order to avoid misunderstanding fo readers when reading this manuscript, in the image showing the mechanism of the photocatalytic process of the material, we would like to change the ZnO material to CS–ZnO/Fe_3O_4 composite material instead of the 3.17 eV energy absorption material to 2.75 eV absorption material to clarify the photocatalytic ability of the material in the visible light region.

Through the above analysis, we can conclude that:

(i) The CS–ZnO/Fe_3O_4 composite material exhibited high photostability under optimal experimental conditions when excited by white LED light. This indicated that the ZnO/Fe_3O_4 nanoparticles were effectively encapsulated by chitosan, which allowed the material to be recovered and reused across multiple photocatalytic cycles.

(ii) Upon photoexcitation, electrons were excited to the conduction band of the CS–ZnO/Fe_3O_4 composite and subsequently migrated to the conduction band of Fe_3O_4. This

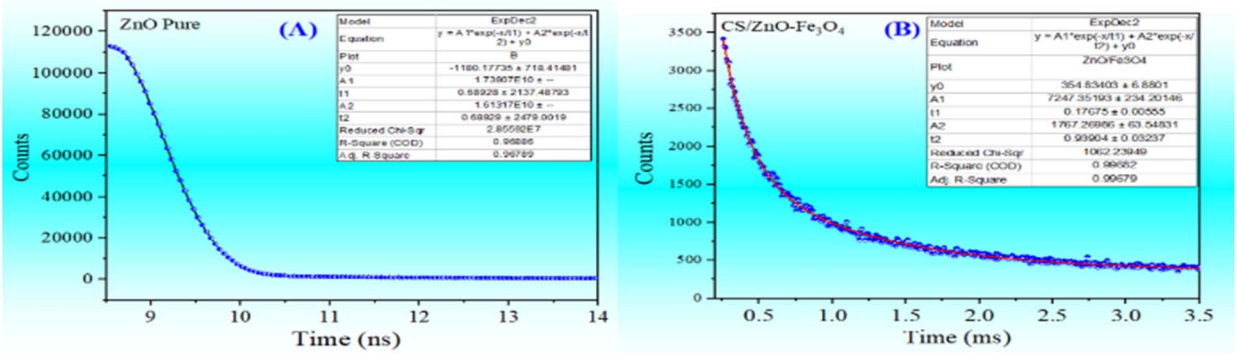

Fig. 15 Lifetime of ZnO (A) and CS/ZnO–Fe_3O_4 (B).

migration process minimized the recombination of electron–hole pairs, thereby extending the lifetime of excited-state electrons in the CS–ZnO/Fe_3O_4 composite compared to pure ZnO. This process protected the material from photocorrosion and enhanced its photocatalytic performance.

4. Conclusions

The synthesis of the ZnO–Fe_3O_4–chitosan (CS–ZnO/Fe_3O_4) three-component composite material was successfully accomplished. CS–ZnO/Fe_3O_4 exhibited a porous surface morphology characterized by nanoparticles with relatively uniform sizes on the nanometer scale. It demonstrated superparamagnetic behavior with a saturation magnetization of 16.95 emu g^{-1}. Moreover, the material exhibited a reduced band gap energy compared to pristine ZnO ($E_g = 3.17$ eV).

CS–ZnO/Fe_3O_4displayed effective photocatalytic degradation capabilities for MO and RhB dyes in water. Optimal conditions for MO removal included a pH of 3, an illumination time of 60 minutes, and a CS–ZnO/Fe_3O_4 mass of 0.15 g. Similarly, for RhB removal, optimal conditions were achieved at a pH of 8, an illumination time of 90 minutes, and a CS–ZnO/Fe_3O_4 mass of 0.15 g. Notably, the efficiency of the photocatalytic degradation process diminished with increasing initial dye concentrations.

The kinetics of MO and RhB degradation by CS–ZnO/Fe_3O_4 conformed to the Langmuir–Hinshelwood pseudo-first-order kinetic model, with the rate constant for MO degradation exceeding that for RhB. Furthermore, CS–ZnO/Fe_3O_4 maintained stable photocatalytic activity even after four reuse cycles.

Data availability

All data generated or analyzed during this study are included in this published article. No additional datasets were used or created. Additional data related to this paper may be requested from the corresponding author xuanvt@tnus.edu.vn.

Author contributions

B. M. Quy: methodology, investigation, writing – original draft, formal analysis, writing – original draft, supervision. N. T. N. Thu, N. T. H. Hoa, N. T. N. Linh, V. Q. Tung, V. T. T. Le, T. T. Thao, N. T. K. Ngan, and N. M. Hung: data curation, formal analysis. L. T. Ha, P. T. Tho and V. T. Xuan: investigation, data curation, formal analysis, writing – review & editing, and editing the final manuscript.

Conflicts of interest

The authors declare that they have no known competing financial interests or personal relationships that could have appeared to influence the work reported in this paper.

Acknowledgements

The research funding from the Ministry of Education and Training (Grant number: B2023-TNA-27) was acknowledged.

References

1 A. A. A. Darwish, M. Rashad and H. A. AL-Aoh, Methyl orange adsorption comparison on nanoparticles: Isotherm, kinetics, and thermodynamic studies, *Dyes Pigments*, 2019, **160**, 563–571.
2 B. Amit, S. D. Sivanesan and C. Tapan, Azo dyes: past, present and the future, *J. Appl. Environ. Biol.*, 2011, **7**, 350–371.
3 A. A. Oyekanmi, A. Ahmad, K. Hossain and M. Rafatullah, Statistical optimization for adsorption of Rhodamine B dye from aqueous solutions, *J. Mol. Liq.*, 2019, **281**, 48–58.
4 S. Gita, A. Hussan and T. G. Choudhury, Impact of Textile Dyes Waste on Aquatic Environments and its Treatment, *Environ. Ecol.*, 2017, **35**, 2349–2353.
5 J. Wu, *et al.*, Magnetically retrievable Fe3O4@SiO2@ZnO piezo-photocatalyst: Synthesis and multiple catalytic properties, *J. Colloid Interface Sci.*, 2023, **636**, 167–175.
6 C. B. Ong, L. Y. Ng and A. W. Mohammad, A review of ZnO nanoparticles as solar photocatalysts: Synthesis, mechanisms and applications, *Renew. Sustain. Energy Rev.*, 2018, **81**, 536–551.
7 S. Goktas and A. Goktas, A comparative study on recent progress in efficient ZnO based nanocomposite and heterojunction photocatalysts: A review, *J. Alloys Compd.*, 2021, **863**(2021), 1–25.

8 M. Muruganandham, *et al.*, Environmental Applications of ZnO Materials, *J. Nanosci. Nanotechnol.*, 2015, **15**, 6900–6913.
9 A. Kolodziejczak-Radzimska and T. Jesionowski, Zinc oxide-from synthesis to application: A review, *Materials*, 2014, **7**, 2833–2881.
10 H. Aliah, *et al.*, Microstructures, Optical, magnetic Properties, and photocatalytic activity of magnetically separable and reusable ZnO-Doped Fe3O4/rGO nanocomposite synthesized via green route, *Carbon Resour. Convers.*, 2024, **7**, 100235.
11 A. Mirzaei, Z. Chen, F. Haghighat and L. Yerushalmi, Hierarchical magnetic petal-like Fe3O4-ZnO@g-C3N4 for removal of sulfamethoxazole, suppression of photocorrosion, by-products identification and toxicity assessment, *Chemosphere*, 2018, **205**, 463–474.
12 W. Cheng, *et al.*, Unraveling the Plasmonic Effect of Au in Promoting Photocatalytic H 2 Generation and Organic Synthesis, *ACS Sustain. Chem. Eng.*, 2024, **12**, 17026–17034.
13 H. Zhang, *et al.*, Metal Sulfide S-Scheme Homojunction for Photocatalytic Selective Phenylcarbinol Oxidation, *Adv. Sci.*, 2024, **11**(17), 1–13.
14 C. Akshhayya, *et al.*, Intimate coupling of 3D MnFe2O4 cubes on 1D ZnO nanorods for sustainable photocatalysis under visible light: Computational analysis of reactive sites and degradation pathway, *J. Taiwan Inst. Chem. Eng.*, 2022, **141**, 104558.
15 A. K. Vishwakarma, B. S. Yadav, A. K. Singh, S. Kumar and N. Kumar, Magnetically recyclable ZnO coated Fe3O4 nanocomposite for MO dye degradation under UV-light irradiation, *Solid State Sci.*, 2023, **145**, 107312.
16 M. Nadafan, M. Sabbaghan, P. Sofalgar and J. Z. Anvari, Comparative study of the third-order nonlinear optical properties of ZnO/Fe3O4 nanocomposites synthesized with or without Ionic Liquid, *Opt. Laser Technol.*, 2020, **131**, 106435.
17 D. Zhang, *et al.*, Recyclable ZnO/Fe3O4 nanocomposite with piezotronic effect for high performance photocatalysis, *Mater. Res. Bull.*, 2022, **148**, 111677.
18 P. T. L. Huong, *et al.*, Efficiency enhancement of photocatalytic activity under UV and visible light irradiation using ZnO/Fe_3O_4 heteronanostructures, *Sol. Energy*, 2023, **249**(2023), 712–724.
19 A. Alasmari, K. Alshehri, A. A. Azab and S. Solyman, Detailed investigation of the structural and electrical properties of ZnO/Fe3O4 nanocomposites, *Phys. Scr.*, 2024, **99**, 035921.
20 A. Manikandan, *et al.*, Structural, morphological and optical properties of multifunctional magnetic-luminescent ZnO@Fe3O4 nanocomposite, *Phys. E: Low-Dimens. Syst. Nanostructures.*, 2020, **124**, 114291.
21 Z. Warren, J. Wenk and D. Mattia, Increased photocorrosion resistance of ZnO foams via transition metal doping, *RSC Adv.*, 2023, **13**, 2438–2450.
22 D. Dworschak, C. Brunnhofer and M. Valtiner, Photocorrosion of ZnO Single Crystals during Electrochemical Water Splitting, *ACS Appl. Mater. Interfaces*, 2020, **12**, 51530–51536.
23 H. Kiziltaş, T. Tekin and D. Tekin, Synthesis, characterization of Fe3O4@SiO2@ZnO composite with a core-shell structure and evaluation of its photocatalytic activity, *J. Environ. Chem. Eng.*, 2020, **8**, 104160.
24 A. M. Smith and S. Nie, Semiconductor Nanocrystals: Structure, Properties, and Band Gap Engineering, *Acc. Chem. Res.*, 2010, **43**, 190–200.
25 C. Karunakaran, P. Vinayagamoorthy and J. Jayabharathi, Nonquenching of Charge Carriers by Fe3O4 Core in Fe3O4/ZnO Nanosheet Photocatalyst, *Langmuir*, 2014, **30**, 15031–15039.
26 B. Erim, Z. Ciğeroğlu, S. Şahin and Y. Vasseghian, Photocatalytic degradation of cefixime in aqueous solutions using functionalized SWCNT/ZnO/Fe3O4 under UV-A irradiation, *Chemosphere*, 2022, **291**, 132929.
27 E. Doustkhah, *et al.*, MOF-derived nanocrystalline ZnO with controlled orientation and photocatalytic activity, *Chemosphere*, 2022, **303**, 134932.
28 A. Reghioua, D. Barkat, A. H. Jawad and A. Saud, Synthesis of Schiff ' s base magnetic crosslinked chitosan-glyoxal/ZnO/Fe3O4 nanoparticles for enhanced adsorption of organic dye: Modeling and mechanism study, *Sustain. Chem. Pharm.*, 2021, **20**, 100379.
29 Q. M. Bui, *et al.*, Removal of Fluoroquinolone Antibiotics by Chitosan–Magnetite from Aqueous: Single and Binary Adsorption, *Processes*, 2023, **11**, 2396.
30 Q. M. Bui, V. D. Nguyen, T. Q. Vu, L. T. N. Nguyen and H. T. H. Nguyen, Removal of anionic dye from aqueous solution by chitosan - magnetite nanocomposite, *Int. J. Environ. Anal. Chem.*, 2022, **00**, 1–21.
31 G. A. Dakroury, E. A. A. El-Shazly and H. S. Hassan, Preparation and characterization of ZnO/Chitosan nanocomposite for Cs(I) and Sr(II) sorption from aqueous solutions, *J. Radioanal. Nucl. Chem.*, 2021, **330**, 159–174.
32 P. Mujeeb Rahman, V. M. Abdul Mujeeb, K. Muraleedharan and S. K. Thomas, Chitosan/nano ZnO composite films: Enhanced mechanical, antimicrobial and dielectric properties, *Arab. J. Chem.*, 2018, **11**, 120–127.
33 V. M. Thanh, *et al.*, Synthesis of ternary Fe3O4/ZnO/chitosan magnetic nanoparticles via an ultrasound-assisted coprecipitation process for antibacterial applications, *J. Nanomater.*, 2020, **2020**, 1–9.
34 F. Tian, *et al.*, A novel magnetic core-shell nanocomposite Fe3O4@chitosan@ZnO for the green synthesis of 2-benzimidazoles, *J. Nanoparticle Res.*, 2017, **19**, 330.
35 J. C. Sin, S. Q. Tan, J. A. Quek, S. M. Lam and A. R. Mohamed, Facile fabrication of hierarchical porous ZnO/Fe3O4 composites with enhanced magnetic, photocatalytic and antibacterial properties, *Mater. Lett.*, 2018, **228**, 207–211.
36 P. Zhang, *et al.*, Preparation and photocatalytic properties of magnetic g-C3N4/TNTs nanocomposites, *Mol. Catal.*, 2019, **465**, 24–32.
37 P. Zhang, *et al.*, Facile fabrication of magnetic Ag/ZnO/Fe3O4 composite and the photocatalytic performance under simulated sunlight irradiation, *Mol. Catal.*, 2021, **508**, 111606.

38 V. T. Le, *et al.*, Efficient photocatalytic degradation of crystal violet under natural sunlight using Fe3O4/ZnO nanoparticles embedded carboxylate-rich carbon, *Mater. Lett.*, 2021, **283**, 128749.
39 H. Huang, *et al.*, Noble-Metal-Free High-Entropy Alloy Nanoparticles for Efficient Solar-Driven Photocatalytic CO_2 Reduction, *Adv. Mater.*, 2024, **36**(26), 1–7.
40 H. Benhebal, *et al.*, Photocatalytic degradation of phenol and benzoic acid using zinc oxide powders prepared by the sol – gel process, *Alexandria Eng. J.*, 2013, **52**(3), 3517–3523.
41 N. Van Kim, N. T. V. Nga, T. T. T. Phuong, N. Le Tuan and V. Vien, Synthesis of g-C3N4/ZnO composites with enhanced photocatalytic activity under visible light, *Vietnam J. Chem.*, 2018, **56**, 220–225.
42 D. Nasuhoglu, V. Yargeau and D. Berk, Photo-removal of sulfamethoxazole (SMX) by photolytic and photocatalytic processes in a batch reactor under UV-C radiation (λmax = 254 nm), *J. Hazard. Mater.*, 2011, **186**, 67–75.
43 J. Xia, A. Wang, X. Liu and Z. Su, Preparation and characterization of bifunctional, Fe3O4/ZnO nanocomposites and their use as photocatalysts, *Appl. Surf. Sci.*, 2011, **257**, 9724–9732.
44 O. Długosz, K. Szostak, M. Krupiński and M. Banach, Synthesis of Fe3O4/ZnO nanoparticles and their application for the photodegradation of anionic and cationic dyes, *Int. J. Environ. Sci. Technol.*, 2021, **18**, 561–574.
45 P. Liu, Y. Liu, W. Ye, J. Ma and D. Gao, Flower-like N-doped MoS_2 for photocatalytic degradation of RhB by visible light irradiation, *Nanotechnology*, 2016, **27**(22), 1–8.
46 P. Raizada, A. Sudhaik and P. Singh, Photocatalytic water decontamination using graphene and ZnO coupled photocatalysts: A review, *Mater. Sci. Energy Technol.*, 2019, **2**, 509–525.
47 A. A. Yaqoob, N. H. B. M. Noor, A. Serrà and M. N. M. Ibrahim, Advances and challenges in developing efficient graphene oxide-based zno photocatalysts for dye photo-oxidation, *Nanomaterials*, 2020, **10**, 1–24.
48 Z. Liu, *et al.*, Preparation of BiOCl/Cu2O composite particles and its photocatalytic degradation of moxifloxacin, *Opt. Mater.*, 2022, **128**, 112432.
49 T. T. Truong, T. T. Pham, T. T. T. Truong and T. D. Pham, Synthesis, characterization of novel ZnO/CuO nanoparticles, and the applications in photocatalytic performance for rhodamine B dye degradation, *Environ. Sci. Pollut. Res.*, 2022, **29**, 22576–22588.
50 H. L. Pham, *et al.* Rational design of magnetically separable core/visible-light photodegradation performance, *RSC Advances*, 2021, 22317–22326.